Stability of finite and infinite von Kármán vortex-cluster streets

Z. Maches, E. Bartley, J. Borjon, and R. Carretero-González

Phys. Rev. E **103**, 032205 — Published 15 March 2021

DOI: 10.1103/PhysRevE.103.032205

Stability of finite and infinite von-Kármán Vortex-Cluster Streets

Z. Maches, E. Bartley, J. Borjon, and R. Carretero-González[1,*]
Nonlinear Dynamical Systems Group[†], [1] *Computational Science Research Center*[‡],
and Department of Mathematics and Statistics, San Diego State University, San Diego, California 92182-7720 USA
(Dated: February 15, 2021)

A wake of vortices with sufficiently-spaced cores may be represented via the point-vortex model from classical hydrodynamics. We use potential theory representations of vortices to examine the emergence and stability of complex vortex wakes, more particularly the von-Kármán vortex street composed of regular polygonal-like clusters of same-signed vortices. We investigate the existence and stability of these streets represented through spatially periodic vortices. We introduce a physically inspired point-vortex model that captures the stability of infinite vortex streets with a finite number of procedurally-generated vortices, allowing for numerical analysis of the behavior of vortex streets as they dynamically form.

I. INTRODUCTION

The traditional von-Kármán (VK) vortex street (VKVS) is a classical problem in wake vortex dynamics and has been analyzed in great detail in existing literature (see, for instance, Refs. [1–4]). It has been shown that the VKVS of alternating, opposite-charge vortices is the only neutrally stable state of two rows of point vortices. More recently, variants of the VKVS have been observed in Bose-Einstein condensates [5, 6]. For instance, it has been observed that instead of producing a VKVS comprised of single vortices at the wake of an impurity [7, 8], a Bose-Einstein condensate produces a vortex street where the single vortices are replaced by rotating, like-charge vortex pairs [5]. Furthermore, vortex streets comprised of vortex pairs have been observed in flapping foils experiments [9]. With the notable exception of the works from Basu, Stremler and co-workers [10–14], the stability of the vortex pair VKVS has not been investigated in great detail, nor have cases of larger, regular polygonal-like vortex clusters. In the present work, we study, within the realm of point-vortex models, the stability of vortex streets comprised of vortex $\mathcal{K}$-gons and examine the changes to parameter space needed to minimize the effects of instability on the street. These vortex configurations correspond to vortex arrays that undergo periodic orbits in an appropriate co-moving reference frame. In Sec. II we consider the traditional, single-vortex VKVS and its regions of neutral stability. Then, in Secs. III through V, we discuss the implementation of a dynamic generation model for single vortex streets and the stability of the created streets. We then discuss in Sec. VI a second method for computing the stability of streets of vortex pairs through a spatially periodic model and discuss the various configurations that lead to neutral stability. Finally, in Sec. VII we further explore cases with larger vortex clusters and relate this to the stability conditions for the vortex pair case.

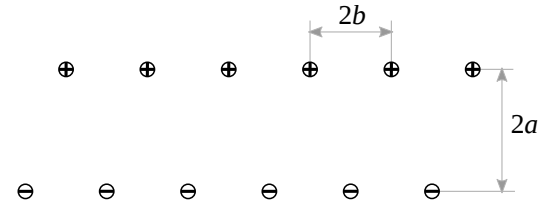

FIG. 1: Von-Kármán vortex street. The topological charge of the vortices denoted by "+" (charge Γ) has equal magnitude but opposite circulation with respect to the vortices denoted by "−" (charge $-\Gamma$).

II. THE STANDARD VON-KÁRMÁN STREET

The VKVS is defined as two parallel interlaced arrays of equidistant vortices bearing, respectively, vortices of topological charge Γ and $-\Gamma$. The (horizontal) spacing between vortices in each array is $2b$ while the (vertical) distance between the arrays is $2a$. The street corresponds to a series of alternating vortices in a zig-zag configuration (see Fig. 1). The line of positively charged vortices is placed on top of the line of negatively charged vortices and thus the inherent velocity of the VKVS is from left-to-right. We consider two particular cases in the present paper: the case of solid walls being imposed on the flow at positions $y = 0$ and $y = 2c$ (see Fig. 2), and the case where the street exists in an unbounded domain (equivalent to the limit as c approaches infinity).

We generalize the VKVS configuration by replacing each individual vortex by a cluster of $\mathcal{K}$ like-charged vortices arranged in a $\mathcal{K}$-gon. For completeness and to justify our analysis, we first discuss the literature results of the standard VKVS where $\mathcal{K} = 1$. The $\mathcal{K} = 1$ street is neutrally stable to perturbations when the ratio between the vertical and horizontal spacings is $2a/(2b) = \coth^{-1}(\sqrt{2})/\pi \approx 0.281$; otherwise, the street is unstable [1]. This so-called Von-Kármán ratio, at which the street is neutrally stable, with some variation due to physi-

*URL: https://carretero.sdsu.edu/
†URL: http://nlds.sdsu.edu/
‡URL: http://www.csrc.sdsu.edu/

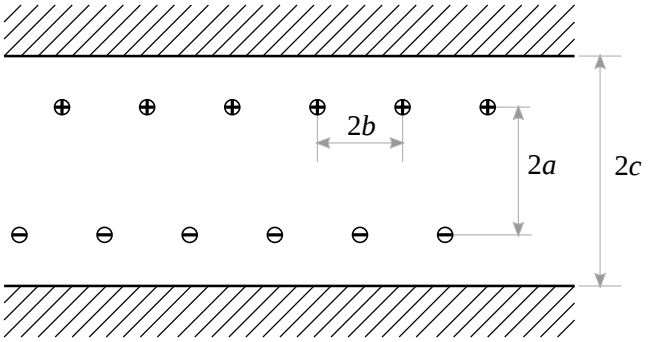

FIG. 2: VKVS in a channel. The parameters of the street are defined such that $2a$ is the separation between the positive and negative vortex arrays, $2b$ the spacing between like-signed vortices, and $2c$ the overall width of the channel.

cal parameters, is seen naturally in systems which show VK vortex shedding for appropriate Reynolds number regimes [15].

Despite the existence of a neutrally stable steady state, it is worth discussing whether it is possible to create a VKVS with a wider range of stability beyond the particular VK ratio. One possible modification to enhance the stability is by imposing boundary conditions onto the fluid, more specifically by creating the street within a confining parallel channel. We refer to the case of a domain that is defined to be unbounded in the horizontal direction and bounded vertically in a strip of width $2c$ to be the channel case (see Fig. 2). For completeness, the analysis of the VKVS in a channel, obtained by Rosenhead in 1929 [4], is summarized below.

To represent the infinite horizontal VKVS in a channel, we fix vortices of charge Γ at the complex valued $(z = x + iy)$ locations $z = 2mb + i(c + a)$, and of charge $-\Gamma$ at $z = (2n - 1)b - i(c - a)$, $\forall m, n \in \mathbb{Z}$. We represent the presence of the channel by the method of images, in order to impose streamlines at the wall locations (i.e., no flux across the channel walls), by adding 'mirror' (opposite sign) vortices to the right hand side of the system of equations whose positions are functions of the corresponding actual vortex positions. The infinite sum of the complex valued potential $\omega(z)$ of channel vortices in the VK configuration may be written as the following infinite sum of a point-vortex lattice [4]:

$$\omega(z) = -\frac{\Gamma a}{2bc} z - \frac{i\Gamma}{2\pi} \ln\left(f\left(\frac{z}{2b}; \frac{a}{2b}\right)\right), \qquad (1)$$

where

$$f(z;\alpha) = \frac{\vartheta_1(z - i\alpha;\tau)\,\vartheta_3(z - i\alpha;\tau)}{\vartheta_2(z + i\alpha;\tau)\,\vartheta_4(z + i\alpha;\tau)}, \qquad (2)$$

where $\vartheta_m(z;\tau)$ is defined as the m^{th} Jacobi theta function and $\tau = 2ic/b$. We note that the Jacobi theta functions, defined through infinite sums, encompass the contribution of the infinite series of mirror images induced by the channel walls.

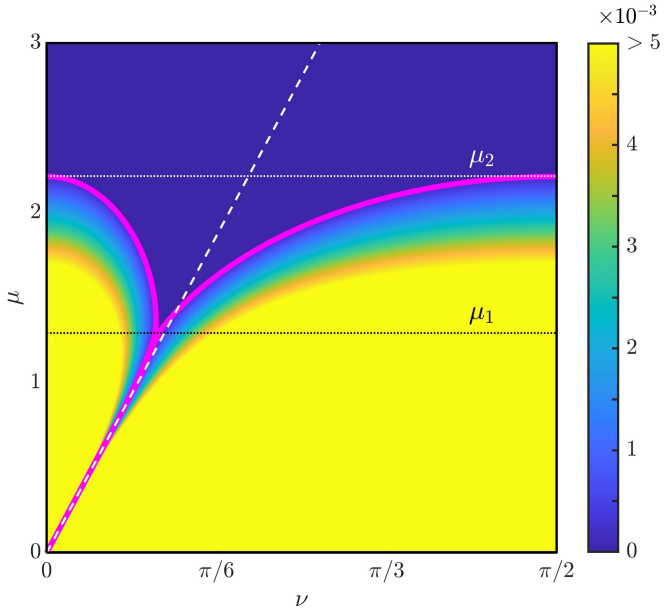

FIG. 3: (Color online) Largest real eigenvalue components of a von-Kármán street in a channel, with the magenta curve delineating the transition to stability [i.e., eigenvalues such that $\mathrm{Re}(\lambda) = 0$]. As the relative horizontal spacing μ increases relative to the channel width, a region of parameter ratios becomes neutrally stable, allowing for more a wider range of physically relevant VKVS configurations. The horizontal black dashed line at μ_1 represents the μ-value above which non-zero areas of stability start to appear while the horizontal white dashed line at μ_2 represents the μ-value above which all configurations are stable. The diagonal dashed white line indicates the von-Kármán stability ratio.

The stability of the VKVS is characterized by the rescaled parameters $\mu = \pi b/(2c)$ and $\nu = \pi a/(2c)$ which represent the previously defined spacing parameters scaled relative to the width of the channel. As all the systems under consideration here are Hamiltonian, for simplicity, we interchangeably use the terms *stable* and *neutrally stable*. The results of the channel analysis are fully explored in Ref. [4], and are replicated in Fig. 3 for $\mathcal{K} = 1$. For low μ and ν values (when the channel walls are far apart relative to the spacing parameters) the behavior of the system recovers that of the unbounded domain case, with neutral stability for a μ and ν ratio equal to the VK ratio. Above a critical μ value, dependent on ν, the system becomes stable. At $\mu = \mu_1 \approx 1.28$ ($b \approx 0.815c$; see horizontal black dotted line) regions of stability in parameter space appear, and at $\mu = \mu_2 \approx 2.23$ ($b \approx 1.419c$; see horizontal white dotted line) the system is stable for all values of a and b (see Fig. 3). In terms of the system, the increasing region of stability corresponds to the relative size of the street growing to a larger scale compared to that of the channel, the walls providing a stabilizing influence on the street. The presence of a channel close to the street relative to the spacing of the street itself permits the vortex

wake to persist for a variety of configurations, providing a broader stability for the region and allowing for a VKVS to persist despite perturbations in its structure. The stability diagram seen here has been reproduced in physical experiments [16], with the added constraint of the vortex width preventing configurations where the vortices are too close to each other or to the walls such that the point-vortex assumption no longer holds.

There has been a significant body of work over the past century discussing the presence, propagation, and instabilities in the classic VKVS, more particularly in cases of finite size (i.e., with an intrinsic width rather than being point-wise) vortices, much of it centered on discussing the modes of the instabilities. It was discovered by Jiménez [17] that the common feature among the inviscid models was the existence of stability only for a particular street parameter value. While attempts have been made to find broader regions, these have been broadly unsuccessful without some external feature such as the restricting channel wall in the work of Rosenhead [4]. While some stable regions were found by Saffman and Schatzman [18] for the pairing instability in finite-sized vortices (which Kármán identified as the most unstable), it was found in the work of Kida [19] and in later sources [20] that, for finite-sized vortices, the pairing instability was not the dominant instability. In the work of Mowlavi et al. [21] the street was found to feature a strong convective instability such that perturbations to the street were carried far enough away from the source that they had little effect on the majority of the street.

For our present analysis, we primarily focus on the presence of instabilities rather than an in-depth consideration of the associated instability modes. The instabilities present in the dynamic generation model are largely the result of asymmetric zig-zag modes. An analysis of the modes becomes more relevant in the discussion of VKVS with $\mathcal{K} > 1$ in Sec. VI. While we do see the appearance of pairing and convective instabilities, we are less focused with the form of the instability and more interested in the existence of stable configurations. Our focus is in the particular geometric structure (i.e., the shape parameters for the different configurations) of the finite and infinite streets that lead to stability. A more detailed discussion of the instability modes and their role in the dynamical destabilization of the steady state configurations is left to future work.

III. DYNAMIC MODEL OF VORTEX GENERATION

From the analysis of the point-vortex street, we have a theoretical system that represents an infinite vortex street (in the horizontal direction) and the stability of its co-moving steady states. Such a system is physically relevant for situations where the street is well-spaced, such that successive vortex cores have minimal influence on each other and, thus, the dominant interaction term between vortices is through the rotation that they induce on the fluid. However, to represent the behavior of vortices generated by an impurity and investigate the stability of the $\mathcal{K} = 2$ case seen in Bose-Einstein condensate models [5], it is not realistic to represent infinitely many independent vortices. Instead, we must consider finite vortex streets (explained in more detail below), where a finite collection of N vortices are positioned in a VK pattern and allow to evolve forward in time. Considering the problem in terms of finitely-many vortices is closer to reality, given that the infinite street will not appear in an actual fluid. We propose a model that qualitatively imitates the generation of a vortex street at the wake of an impurity through baroclinic effects via a system of ODEs which will allow for increased understanding of the dynamics of the vortex street and its evolution.

Consider a system of N point vortices located in some domain, either infinite in all directions or in a channel, at positions z_k, $k \in \mathbb{Z}_N$. Let us represent the motion of the k^{th} vortex by

$$\frac{d\bar{z}_k}{dt} = \frac{dx_k}{dt} - i\frac{dy_k}{dt} = F_k(z_1, ..., z_N), \tag{3}$$

where F_k is a nonlinear function of the positions of all vortices. In the case of the, no channel, unrestricted domain (which we call from now on the unbounded domain case), the dynamics of interacting point vortices is described by the following velocity terms [22]

$$F_k(z_1, ..., z_N) = \frac{1}{2\pi i}\sum_{j=1, j\neq k}^{N} \frac{\Gamma_j}{z_k - z_j}. \tag{4}$$

On the other hand, when the vortices are placed in a channel of finite width with the walls at $y = 0$ and $y = 2c$, one can apply the method of images [23] to obtain the following velocity terms [24]

$$F_k(z_1, ..., z_N) = \frac{i\Gamma_k}{8c}\coth\left(\pi\frac{z_k - \bar{z}_k}{4c}\right) - \sum_{j\neq k}^{N}\frac{i\Gamma_j}{8c}\left[\coth\left(\pi\frac{z_k - z_j}{4c}\right) - \coth\left(\pi\frac{z_k - \bar{z}_j}{4c}\right)\right].$$

Each of these equations forms a system of N complex, nonlinear ODEs, which may be solved numerically by considering either the complex system or the corresponding $2N$ system in Cartesian coordinates, such that

$$\frac{dx}{dt} = \text{Re}\left(\frac{dz}{dt}\right), \tag{5}$$

$$\frac{dy}{dt} = -\text{Im}\left(\frac{dz}{dt}\right). \tag{6}$$

Vortices are generated by assuming a constant background velocity, corresponding to a situation where a constant right-to-left flow passes around a stationary impurity (which is equivalent to an obstacle moving to the

right though a stationary fluid). In addition to the background flow (at constant velocity), we add, at regular time intervals, vortices at positions z_+ and z_- corresponding to the street we are creating. For a $\mathcal{K} = 1$ VKVS, the seeding would occur at $z_\pm = i(c \pm a)$, with the seeding time being determined by the background velocity and the b parameter. Whether a generated street takes the form of a parallel (rectangular) or antiparallel (zig-zag) configuration depends on whether the vortices at z_+ and z_- are generated at the same time (parallel) or in an alternating fashion (antiparallel). Horizontal spacing, represented by b, is determined by (ignoring again vortex-vortex interactions) both the time between alternating (top and bottom) seedings and the background horizontal velocity. As we consider a background flow at a fixed right-to-left velocity v around a stationary obstacle, in order to maintain the b vortex spacing, b and the background velocity may be used to determine the time between seedings t_s with the relationship $2vt_s = b$.

We can further generalize the algorithm for any regular pattern of vortex generation. At the end of each interval, we introduce some number of new vortices at predetermined locations, and integrate the system forward based on the relative interactions between the vortices, the background flow, and the boundaries of the system. From results seen in the literature [25], we also assume the vortex is created fully formed at a sufficient distance away from the obstacle so as to minimize the influence of the obstacle on the flow, which is valid for vortices of sufficient distance from the point of origin. Therefore, from this point forward, we neglect the dynamical effects exerted by the impurity and, thus, it is not directly included in the model and it is not depicted in Fig. 4 (nor in Fig. 10).

It is important to mention that, per construction, when no background flow nor impenetrable walls are considered, the VKVS on its own moves left-to-right (i.e. towards the fictitious impurity) while the background flows in the opposite direction. Furthermore, the net effect of the impenetrable walls is to slow down the intrinsic velocity of the VKVS. The combination of these three effects (intrinsic VKVS speed, effects of the walls, and background flow) results on a combined right-to-left VKVS velocity when measured in the stationary frame (in which the impurity is fixed at $x = 0$).

IV. VORTEX STREET PARAMETERS

For a system generated dynamically, it is worth considering the role that the finite and dynamic nature of the system plays in determining the street spacing parameters a and b (i.e., ν and μ in the channel case). Nonlinear interactions between vortices in the system render it analytically impossible to determine the asymptotic (final) spacing values. We define the a-priori estimates, corresponding to the original locations where we seed the vortices, as a_{ini} and b_{ini}, and we evaluate the settled values a_{fin} and b_{fin} when the VKVS has settled. To allow for the dynamic adjustment of the VKVS parameters, we allowed the system to run long enough to generate a large number of vortices and define the estimates for a_{fin} and b_{fin} (correspondingly μ_{fin} and ν_{fin} in the presence of the channel) given a large enough subset of the vortices. This subset was determined to be all vortices (excluding the two most recent) within a vertical deviation tolerance from the other vortices in the subset. After some testing, we chose an arbitrary tolerance of $0.005c$ (c being the half-width of the channel). We found that varying this tolerance does not significantly affect the results that follow, thus, from now on the tolerance is set to $0.005c$. An example of the dynamical procedure generating a stable wake is depicted in Fig. 4 where the vertical dashed lines bound the region of the converged subset of vortices. The parameter updating procedure was repeated for varying numbers of vortices to find an ideal number of vortices after which the parameter shifting did not noticeably change, which, as shown in Fig. 5, is around fifty vortices. These updated estimates for the spacing parameters are the parameters we use in all of our subsequent results.

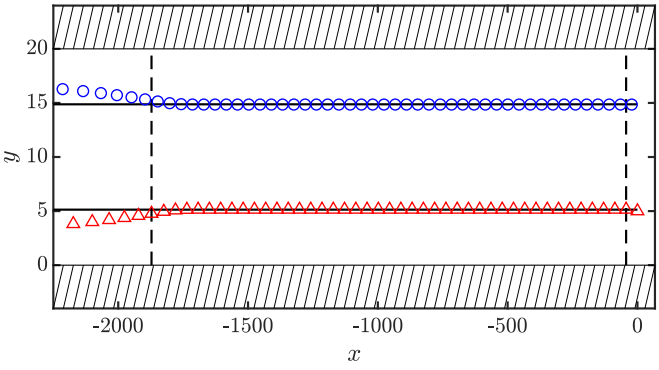

FIG. 4: (Color online) Dynamical generation of a (stable) von-Kármán vortex wake inside an impenetrable channel (hashed regions). The vortices are initially seeded at $x = 0$ (location of the fictitious obstacle) and move to the left following the background velocity of the fluid. Blue (Red) circles (triangles) represent vortices with positive (negative) charge. To estimate the width (see horizontal lines) of the street we consider vortices with a y position within a tolerance of $0.005c$ of the final (average) vertical location of the street. Here $\mu = 2.5$, $\nu = \pi/4$, and $c = 10$. Vortices between the two vertical dashed lines are considered inside the von-Kármán vortex configuration. It is clear from the figure that the selected vortices form a reasonable approximation of a consistent von-Kármán vortex street.

Let us now study in more detail the relation between the estimated (seeded) shape parameters (a_{ini} and b_{ini}) determined by the dynamical vortex seeding and the converged shape parameters (a_{fin} and b_{fin}). Our dynamical model seeds the vortices at $(0, c \pm a_{\text{ini}})$ every t_s time units yielding $b_{\text{ini}} = 2vt_s$. It is important to note that the final values a_{fin} and b_{fin} depend on the background velocity and the channel width. For instance, Fig. 6 de-

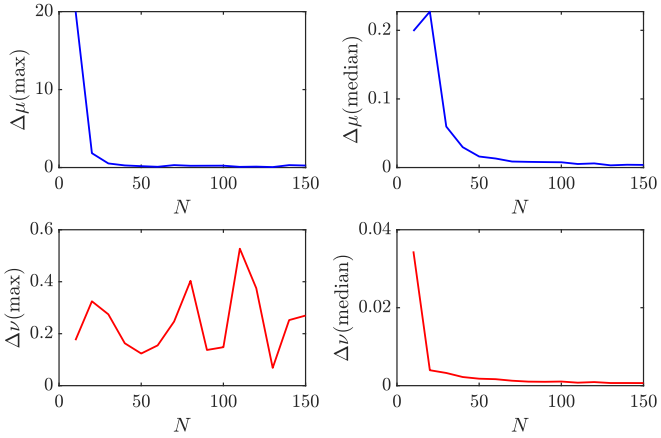

FIG. 5: Maximum change in estimates for μ and ν values after seeding N number of vortices for μ between 0.5 and 3 and ν between 0.1 and $\pi/2$. Top (bottom) panels depict results for μ (ν). Left (right) panels show the maximum (mean) deviation. We see that after about fifty vortices are seeded, the change in the estimated parameters is minimal. The only exception, see bottom-left panel, is the maximum deviation for ν, $\Delta\nu$, which does not seem to converge as N increases.

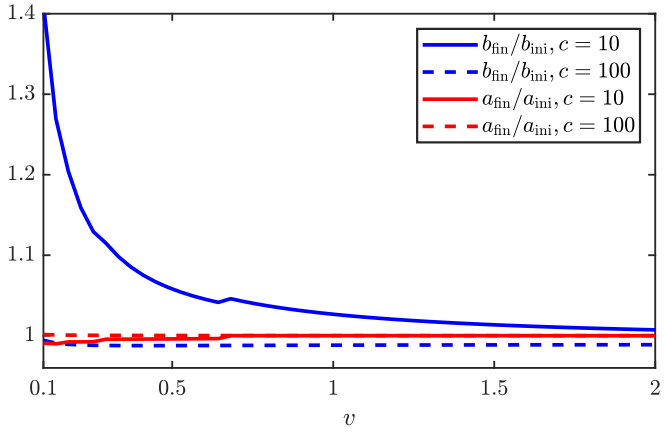

FIG. 6: (Color online). Convergence of the VKVS spacing parameters a and b as a function of the right-to-left background velocity v for two channel widths ($c = 10$ and $c = 100$). We depict the ratios $b_{\text{fin}}/b_{\text{ini}}$ (blue curves) and $a_{\text{fin}}/a_{\text{ini}}$ (red curves) for $c = 10$ (solid curves) and $c = 100$ (dashed curves) with $b_{\text{ini}} = 19.1$ and a_{ini} chosen at the von-Kármán ratio. The results are plotted after 100 vortices were seeded. The final spacing parameters tend to their initial counterparts as both the background velocity and the channel width increase.

picts the dependence of the final values (as ratios with their initial counterparts) as the background velocity is increased for the case of a narrow ($c = 10$) and a wide ($c = 100$) channel. In all of these results we chose a_{ini} and b_{ini} at the von-Kármán ratio to ensure a stable formation of the VKVS. The results in the figure show that the b shape parameter (horizontal spacing) has a strong dependence on the background velocity and the channel width. In contrast, the a shape parameter (vertical spacing) has a much weaker dependence on the background velocity and the channel width ($|a_{\text{fin}}/a_{\text{ini}} - 1| < 0.01$). As the background velocity v is increased, both a_{fin} and b_{fin} tend to their initial counterparts. The main effect of the presence of the channel is to (through the interaction of the vortices with their opposite-signed images emulated by the impenetrable walls) speedup the downstream vortices. This effect results in the stretching of the horizontal distance between vortices which, in turn, results in an increase of the ratio $b_{\text{fin}}/b_{\text{ini}}$. Note that a wide channel (cf. see dashed curves for the $c = 100$ case in Fig. 6), having a weaker influence on the forming vortex street, results, naturally, in relatively small variations between the initial and final values of the shape parameters. For simplicity, as here we are only concerned with the final (converged) shape parameters, in what follows we drop the "fin" subindex used in the shape parameters in the previous section. Namely, from now on, $\nu_{\text{fin}} \to \nu$ and $\mu_{\text{fin}} \to \mu$.

Finally, let us comment on the velocity for the front and back ends of the street. We refer to the "front end" of the street as the side furthest from the seeding point, and the "back end" the side closest to it. We monitor the position of the front and back ends with time using the horizontal extent limits of the forming VKVS as defined above; see positions of the vertical dashed lines in Fig. 4. From these positions we compute the respective average velocities until hundred vortices are seeded (and discarding a short initial transient). Our simulations reveal that, after a short initial formation period, the back end of the VKVS remains practically stationary. This consequently slaves the vertical spacing of the street to the seeding process and, thus, precludes noticeable variations in a_{fin}. As for the front end, we found that, generally, its velocity was essentially equivalent to the background velocity, with deviations becoming more pronounced in unstable street cases. The deviations in these unstable cases were the result of decreasing front end velocities signaling the progressive destruction of the street at the front end towards an irregular (chaotic) wake (see for instance Fig. 10 where an unstable VKVS "sheds" vortices in its wake that, in turn, accelerates its destabilization).

V. FINITE STREET RESULTS

With the stability of the ideal $\mathcal{K} = 1$ case extensively addressed in the literature, we now examine the results of the finite model for both the unbounded domain and channel cases. The method of generation is the one introduced above; spacing parameters, background velocity, and the channel width are varied while all other features held constant. We consider all point vortices to have topological charge $\Gamma = \pm 1$.

To compute the stability of the dynamically generated street, we build the numerical Jacobian along vortex street trajectories. We create the Jacobian by first iteratively constructing the street by the successive gen-

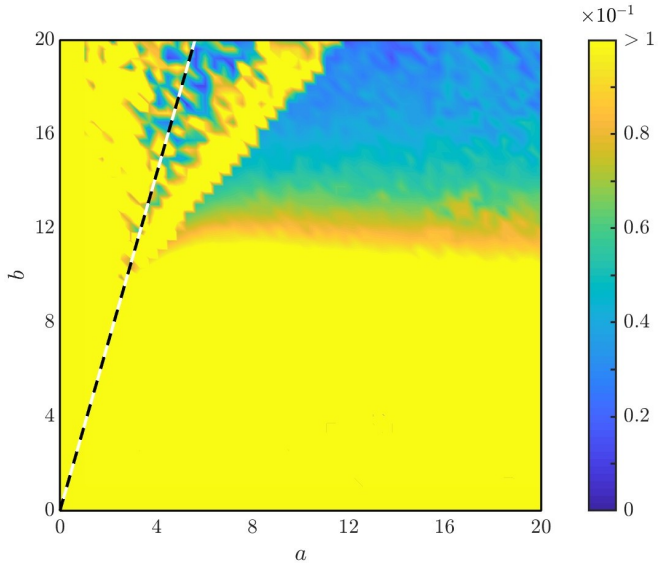

FIG. 7: (Color online) Stability diagram of the dynamically generated $\mathcal{K} = 1$ vortex street in an unbounded domain across the parameter space determined by the a-priori initial estimates of the spacing parameters, with background velocity $v = 0.1$. Depicted is the corresponding maximum real eigenvalue component of the stability spectrum. The system is clearly unstable in such a fundamental way that the traditional structure of the VKVS does not fully display the characteristic VK ratio (see dashed line) except for higher parameter values.

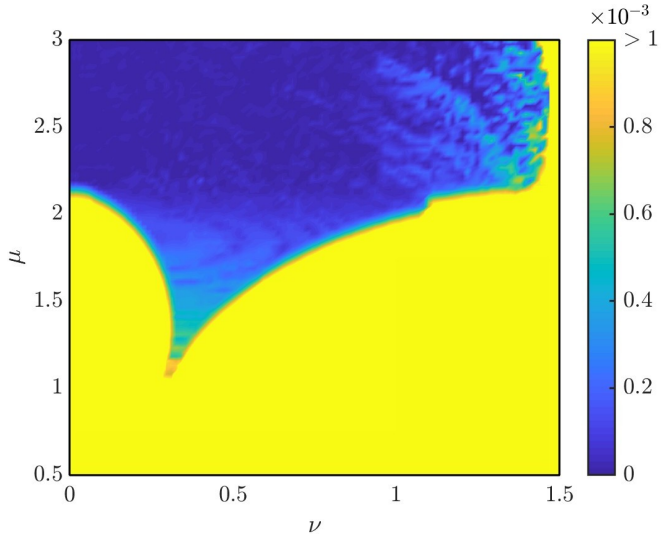

FIG. 8: (Color online) Stability diagram for the dynamically generated $\mathcal{K} = 1$ vortex street in a channel of width $2c = 20$.

eration of vortices. Once the street has been formed, we successively apply a small perturbation to each position variable, allow the street to develop for a fixed time interval, then map the vortices back by their overall average horizontal displacement, compute the difference between the initial and final positions, and from there estimate the entries of the associated numerical Jacobian. This allows us to analyze the stability of the street on a comoving reference frame in which the VKVS is a fixed point. Though the true fixed point only exists for an infinitely long street, the numerical Jacobian approach used here will converge to the results of the infinite street given a sufficient number of vortices. Tantamount to the spacing parameters convergence observed in Fig. 5, we also find that the eigenvalues extracted from this numerical Jacobian exhibited little variance after fifty vortices had been generated. We thus extract the maximal real eigenvalue component from this procedure as a measure of the trajectory's stability. If the largest unstable eigenvalue is of sufficiently small magnitude, the destabilization will only become noticeable after a significant amount of time elapses. As we do not expect a real VKVS to continue indefinitely (due to any number of physical boundary conditions or flow features), we consider the street to be effectively stable if the largest real eigenvalue is relatively small.

Plotting the stability diagram for the unbounded domain case, we do see in Fig. 7 a decrease in the size of the largest real eigenvalue, corresponding mainly to an increase in the spacing parameters. The correlation between a finite collection of vortices spaced far apart and the effect of perturbations on the structure of the vortices as a whole is clear: with a finite number of vortices, the effect of increasing the vortex-vortex spacing is to decrease the effect of any one vortex on all others, indicating that whether or not the vortices do form a VKVS, the perturbations have little effect. For high a and b values, despite the presence of some instabilities, we do see traces of the expected VK ratio. This indicates that, even in the case of vortices generated one at a time in an unrestricted domain, the VK stability ratio is still present.

For the horizontally finite $\mathcal{K} = 1$ case in a channel, we consider stability in terms of the scaled parameters μ and ν. The stability diagram for the finite vortex street case in a channel of width $c = 10$ is depicted in Fig. 8. We find that for values that correspond to highly unstable vortex streets, maximum real eigenvalues fall on the order of 10^{-3}, and for those where the only instability is the expected unwinding at the free end of the street, the maximum eigenvalues are on the order of 10^{-5}. As a result, we consider eigenvalues of around 10^{-4} as the boundary between in-practice stable and unstable regimes. As seen in Fig. 8, by considering eigenvalues above 10^{-3} as unstable, the reconstructed parameter sweep strongly mimics the results for the ideal, infinite, VKVS (see Fig. 3).

As depicted in Fig. 9, we further note that the number of vortices that converged in a VKVS configuration within vertical tolerance of $0.005c$ had a similar qualitative distribution as the one displayed by the stability diagram. The final a and b (or ν and μ) values are most accurate when a large percentage of vortices are in a street structure which corresponds to a stable case. A low number indicates a relatively small sample size

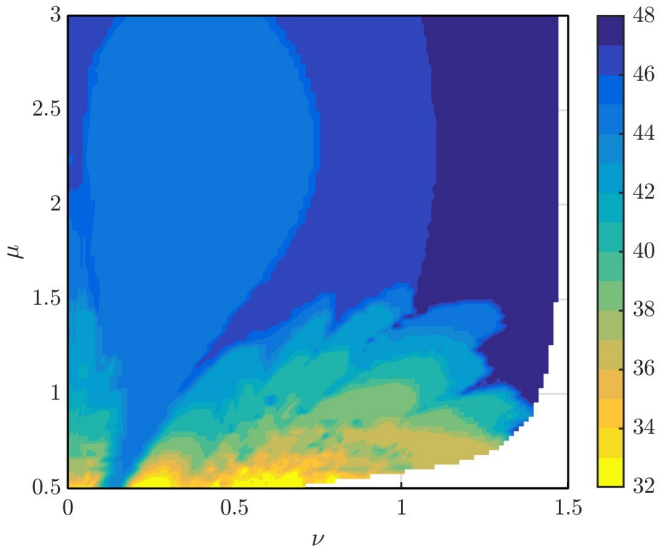

FIG. 9: (Color online) Number of vortices used in creating the updated μ and ν estimates, for fifty seeded vortices. We note that in the more stable region, a majority of the vortices are within vertical alignment tolerance $0.005c$ of each other, supporting that not only are the results stable, but that they form a well-established VKVS.

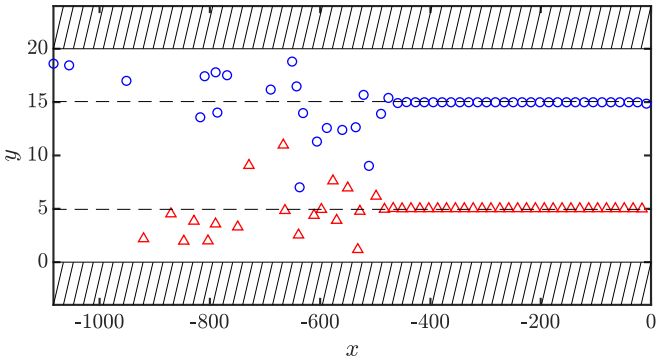

FIG. 10: (Color online) An example of a von-Kármán vortex wake generated dynamically inside an impenetrable channel (hashed regions). The vortices are initially seeded at $x = 0$ (location of the fictitious obstacle) and move to the left following the background velocity of the fluid. The particular case corresponds to an unstable wake for an initial vortex seeding with $\nu = \pi/4$ and $\mu = 0.5$. Compared to the stable wake seen in Fig. 4, we see that although both wakes retain some degree of the von-Kármán structure, the unstable one develops a disordered (chaotic) wake after a certain distance while the stable one is essentially preserved in its entirety. The horizontal dashed lines mark vertical positions of the converged vertical spacing. Of the two scenarios, clearly the unstable case has fewer vortices within the von-Kármán configuration, while the majority of the vortices in the stable case can be considered in a von-Kármán configuration.

to make any fair estimate. It also implies minimal adjustment of the parameter near the point of generation. For stable cases, relatively large number of vortices are used, while for unstable cases, fewer contribute to the "von-Kármán" street (see also Fig. 10). We also note in Fig. 9 that the number of vortices within tolerance for stable cases is significantly higher than for unstable ones, and that the majority of these cases seems to be for high μ and ν values, where the dominant effect on the vortices would be from the channel influence (and thus lower chance for instability).

In Fig. 10 we depict a characteristic example of a wake for an unstable street in the channel. There is a clear difference between the stable wake depicted in Fig. 4 and the unstable one in Fig. 10, marked by the behavior in the tail-end of the street. The impact of the channel walls appears to effectively stabilize the tail-end of the street. Interestingly, the effect of the channel's nearest wall on a seeded vortex is to increase its velocity away from the point of origin. Thus, vortices that break from the street formation in stable cases will move further away from the street, minimizing the effect the divergent vortex has on the street as a whole. Example eigenvalue spectra for stable and unstable wakes are depicted in Fig. 11. The spectra, computed using the numerical Jacobian as explained above, display a symmetric distribution across both axes, which is the expected distribution for a Hamiltonian system. Nonetheless, it is important to mention that we are computing the numerical Jacobian on a *subset* of vortices as explained above and, thus, the subsystem under consideration, is not strictly Hamiltonian. As it can been seen from the inset zoom in the stable case (bottom panel), there are roughly four orders of magnitude separating the size of the largest real eigenvalue component when comparing the stable (bottom panel) and unstable (top panel) cases.

Let us now discuss the impact of vortex street velocity on the system as a whole. If we consider two arbitrary vortices at some distance d apart, we note that as the distance between the two increases, the mutual effects on their velocity converges to zero at a rate $1/d$. Thus, for any configuration of vortices in a channel, the infinite images created by the system and the others will have little noticeable effect after a certain distance, leaving the background velocity as the dominant term. While in the infinite street case the background velocity is a constant dependent on the parameters, the finite case will instead have its velocity converge to zero as the strength of the vortex-vortex interactions diminishes the further apart the vortices are positioned.

Finally, it is relevant to mention that, in contrast to the infinite street case, for the finite street case, varying the channel width does have an effect on the stability of the system even in the normalized μ and ν shape parameters. The effects can be attributed to the finiteness of the model, where, unlike in the infinite street, proximity to the walls have an unbalanced effect between the bulk and the tail-end of finite street. Seeding the vortices with parameters relative to a wider channel will minimize the overall influence of the vortices on each other and, thus, lessening the influence of instabilities.

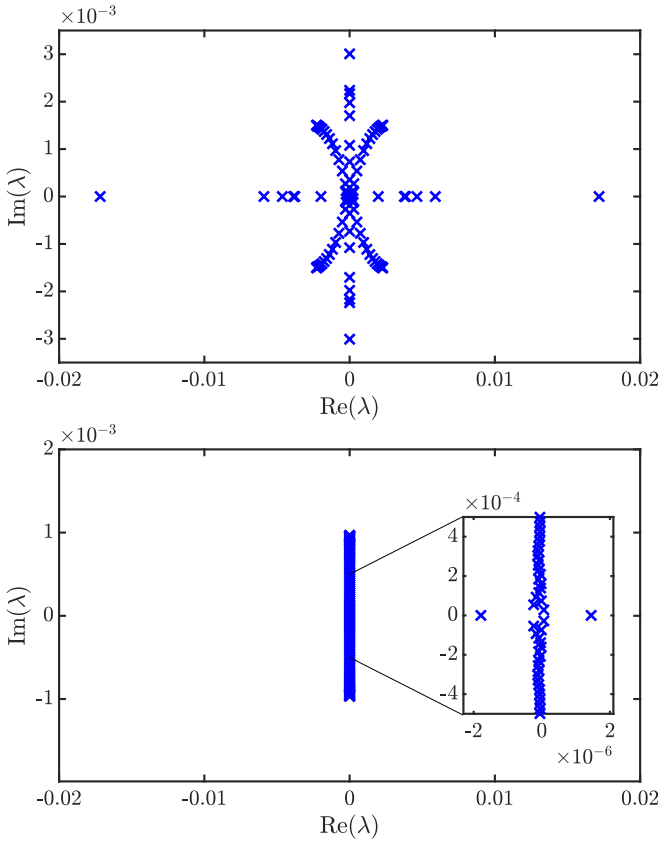

FIG. 11: Typical eigenvalue distributions for the unstable ($\mu = 1, \nu = \pi/4$; see top panel) and stable ($\mu = 3, \nu = \pi/4$; see bottom panel) cases of a dynamically generated (finite) VKVS. The symmetry across the axes is a consequence of the near Hamiltonian structure of the underlying system.

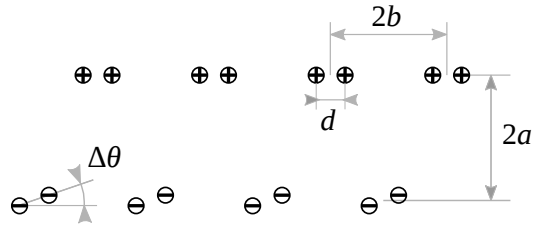

FIG. 12: An example $\mathcal{K} = 2$ vortex street. Note that a and b are now defined to be the vertical and horizontal spacings between the centers of vortex pairs instead of the spacings between vortices themselves. We also see the addition of new parameters d, which refers to the diameter of a vortex pair within the street, and $\Delta\theta$, which indicates the relative angle of rotation between the positive and negative pairs.

VI. PERIODIC MODEL RESULTS FOR $\mathcal{K} > 1$

A VKVS configuration with $\mathcal{K} > 1$ is composed of $\mathcal{K}$-gons (of radius $r = d/2$ and centered at the positions of the original $\mathcal{K} = 1$ vortices) of evenly spaced point vortices that replace the original individual vortices for the $\mathcal{K} = 1$ case. The vortex clusters in turn, for sufficiently small radius relative to a and b, act on the other clusters as a single vortex of charge $\mathcal{K}\Gamma$, causing the street as a whole to move horizontally like in the $\mathcal{K} = 1$ case with time rescaled by Γ. It is important to note that it has been shown in the literature that an isolated $\mathcal{K}$-gon configuration is only stable for $\mathcal{K} \leq 7$ (see Refs. [26–28]). As a result, there exists a hard upper limit on the possible stable streets that can be created. We consider as a base case the $\mathcal{K} = 2$ configuration as depicted in Fig. 12. Note that a $\mathcal{K} > 1$ VKVS will possess at least two new parameters: the diameter d of the $\mathcal{K}$-gon and the relative angle $\Delta\theta$ between the positively and negatively charged $\mathcal{K}$-gons.

As before, the $2a$ and $2b$ respectively denote the vertical and horizontal spacings of the pairs, while a new parameter r is introduced to define the radius of the single like-signed vortex cluster. We may further consider the parameters $2c$ (defined as before to be the channel width) and $\Delta\theta$ (defined to be the difference in rotational angle between positive and negative vortex pairs). In addition, the $\mathcal{K} > 1$ case does not typically exhibit steady states even in a co-moving reference frame (the principal exception being the $\mathcal{K} = 2$ case where $b = d$ and $\Delta\theta = 0$, which is a street of parallel vortices shown to be universally unstable [1]). Rather, in a co-moving frame the $\mathcal{K} > 1$ case displays periodic orbits corresponding to the rotation of the like-signed vortex pairs. Due to the intrinsic nonlinearity of the problem, it is difficult to produce analytical stability results for these nonlinear periodic orbits on a co-moving reference frame. Therefore, we rely on a numerical strategy based on elementary unit cells. We define a periodic, unit, cell to be a portion of the infinite street of horizontal width $2b$ containing one positive and one negative sign cluster, with periodic boundary conditions to the left and right. In particular, for the unbounded domain, the equations of motion may be obtained as the sum of the equation for a single periodic point vortex obtained from Refs. [11, 29], and takes the general form

$$\frac{d\bar{z}_k}{dt} = \frac{1}{4bi} \sum_{j=1, j\neq k}^{N} \Gamma_j \cot\left(\frac{\pi}{2b}(z_k - z_j)\right). \qquad (7)$$

On the other hand, for the channel case, we recall that the equations used by Rosenhead to model the VKVS in a channel represent two vortices in predetermined positions repeated periodically in the x-direction every $2b$ distance. Following the derivation in Rosenhead [4] for a single vortex of arbitrary position z_k, it is straightforward to show that the equations of motion for N point vortices

repeated periodically in a channel take the form

$$\frac{d}{dz}\omega_k = \frac{1}{4b\pi}\sum_{j=1,j\neq k}^{N}\Gamma_j\left(\frac{4\pi}{\tau}(\bar{z}_j - z_j) - i\frac{\vartheta_1'(\frac{1}{2b}(z_k-z_j);\tau)}{\vartheta_1(\frac{1}{2b}(z_k-z_j);\tau)} + i\frac{\vartheta_4'(\frac{1}{2b}(z_k-\bar{z}_j);\tau)}{\vartheta_4(\frac{1}{2b}(z_k-\bar{z}_j);\tau)}\right). \tag{8}$$

With the notable exception of the works of Basu, Stremler and co-workers [10–14], there is little explicit literature on the $\mathcal{K}=2$ case. Therefore, let us numerically tackle the stability analysis of the $\mathcal{K}=2$ configuration, both in an unbounded domain and in a channel, through the lens of point-vortex models. To examine the stability of the $\mathcal{K}=2$ street, we find periodic orbits for streets with various values of a, b and d, by integrating forward a single expected period, correcting for average displacement of mass, and computing as error how far the corrected value is from the initial point on the orbit. To find a "true" orbit, we minimize the error using a standard nonlinear least square numerical procedure.

It is crucial to note that, because of periodicity, not only configurations are periodic but also are their respective perturbations. Thus, any perturbation in the cell corresponds to a periodic perturbation of the infinite street across *all* cells. Therefore, to consider perturbations with non-trivial y dependence (i.e., not only homogeneous across all cells due to periodicity), we must consider instead the system of vortices created by horizontally concatenating n unit cells and adjusting the period to be $2bn$ in the x direction.

A. Existence of Periodic Orbits

Before studying the stability of the $\mathcal{K}=2$ configuration, let us briefly comment on its regions of existence. Figure 13 depicts the families of $\mathcal{K}=2$ periodic orbits (in their corresponding co-moving reference frame) for $\Delta\theta=0$ (top) and $\Delta\theta=\pi/2$ (bottom) for different values of the distance d between vortices in each pair and while keeping the shape parameters a and b constant. As it can be seen from the figure, relatively small d values (when compared to the b) result in almost circular orbits as the positively and negatively charged vortex pairs are relatively distant from each other and thus interact weakly. However, as d is increased, the vortex pairs interact more strongly and the orbits deform into configurations with a triangular-like shape. As d is increased further, our optimization routine is unable to converge suggesting the existence of a maximum threshold value above which $\mathcal{K}=2$ solutions cease to exit. In fact, as d increases, there will be a threshold value when vortices across pairs will be closer than in their own pair. For $\Delta\theta=0$, as the orbits are symmetric with respect to the origin, this critical distance d_c corresponds to the minimum between (i) $d_c=\sqrt{4a^2+b^2}$ (distance between opposite signed-vortices across pairs) when $a<\sqrt{3}b/2$ and (ii) $d_c=2b$ (distance between same signed-vortices across pairs) when $a>\sqrt{3}b/2$. For the parameter values of Fig. 13 ($a=1$ and $b=3/2$; i.e., $a<\sqrt{3}b/2$) this happens at $d_c=\sqrt{4a^2+b^2}=5/2$. For $\Delta\theta=\pi/2$, the traces of the orbits are indeed symmetric with respect to the origin (see bottom panel in Fig. 13), however the orbits themselves do *not* follow this symmetry as the orbit of the positively-charged pair is shifted by half a period with respect to the orbit of the negatively-charged pair. Therefore, the critical distance in this case cannot be computed a-priori. Nonetheless, we have checked that our optimization routine ceases to converge at $d_c\approx 2.91$ which is precisely when the inter pair distance is equal

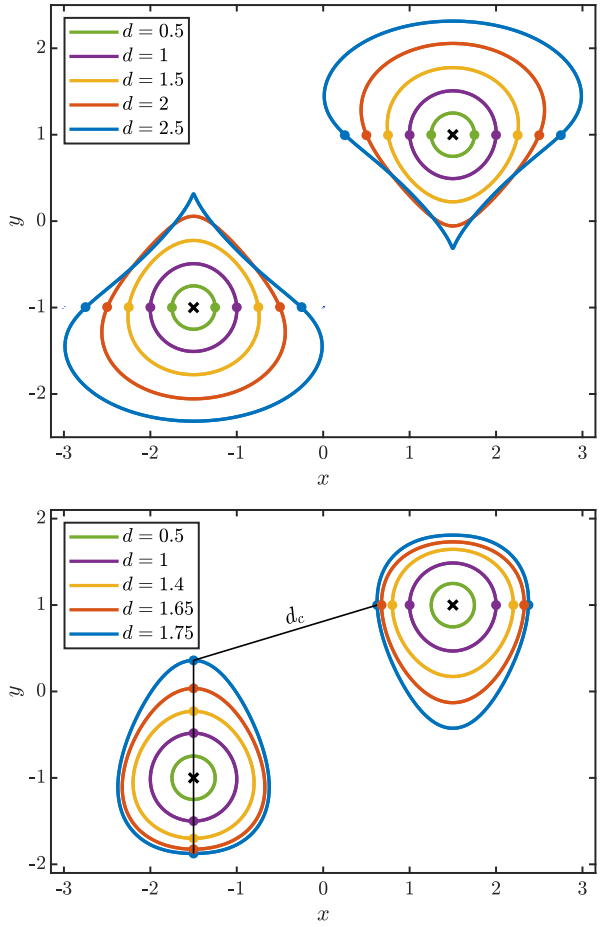

FIG. 13: (Color online) $\mathcal{K}=2$ von-Kármán trajectories in a unbounded domain plotted in a co-moving reference frame for $a=1$, $b=3/2$, and $\Delta\theta=0$ (top) and $\Delta\theta=\pi/2$ (bottom). The different orbits correspond to different values for the initial inter-vortex pair distance d (measured on the top-right pair). Initial conditions are depicted with circles. The VKVS velocities for the $\Delta\theta=0$ case (top) correspond to $v=-0.1301$, -0.1300, -0.1297, -0.1293, and -0.1307, for, respectively, $d=0.5$, 1, 1.5, 2, and 2.5, while for the $\Delta\theta=\pi/2$ case (bottom) they correspond to $v=-0.1301$, $v=-0.1295$, $v=-0.1274$, $v=-0.121$, and $v=-0.107$ for, respectively, $d=0.5$, 1, 1.4, 1.65, and 1.75.

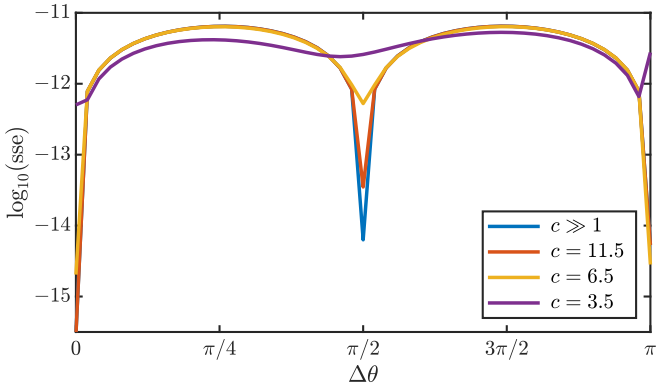

FIG. 14: (Color online) Convergence residual of a $\mathcal{K} = 2$ orbit for $a = 1$, $b = 10$, and $d = 1$ as $\Delta\theta$ is varied, for multiple channel widths. Depicted is the logarithm of the sum of square errors (sse) on our optimization routine as a function of $\Delta\theta$. Clearly, in the wide channel limit, the only valid orbits are for $\Delta\theta = k\pi/2$, as convergence is poor elsewhere. Contracting the channel eventually destabilizes even the $\pi/2$ case.

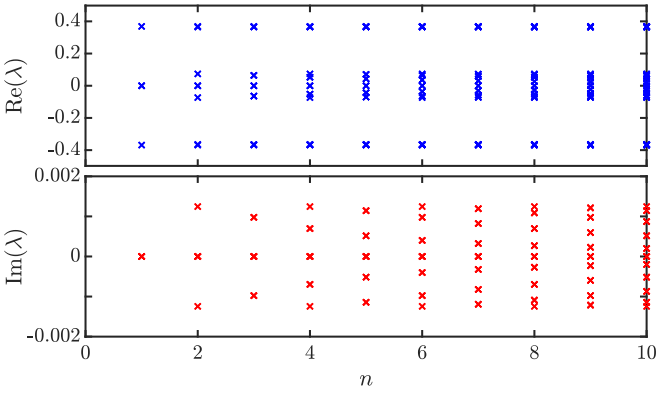

FIG. 15: Dependence of the spectral stability on the number n of units cells used in the model. Real (top) and imaginary (bottom) eigenvalue spectra for $d = 1$, $a = b = 2.3673$. We see that, after relatively few cells, the maximal real components of the eigenvalues show good convergence.

to the distance across pairs (see thin dark lines in the bottom panel of Fig. 13).

On the other hand, let us briefly study the existence of $\mathcal{K} = 2$ configurations as the channel wall width and the relative angle between vortex pairs $\Delta\theta$ are varied. In particular, as observed in Fig. 14, convergence to the steady state is hindered when the channel walls get tighter into the vortex street configuration. Namely, when the channel width $2c$ gets closer to the vortex street width $2a + d$. This is a direct consequence of the effects induced by the mirror image vortices introduced by the channel wall which preclude the vortex pairs to follow their natural rotation. On the other hand, we find that convergence to a periodic state is enhanced when the symmetry of the orbits is preserved. Namely, when the relative angle between positive and negative pairs, $\Delta\theta$ is such that $\Delta\theta = k\pi/2$, $\forall k \in \mathbb{Z}$.

B. Floquet Stability Analysis

To compute the stability spectrum of the numerically found periodic orbits in the co-moving reference frame, we call on the method of Floquet analysis (see Ref. [30] and references therein). The analysis is motivated by the need to adapt the methods for computing the stability of a steady state to a system which, in a co-moving frame, has a periodic orbit. We can adapt these methods by computing the effects of small perturbations on the trajectory *over one period* and, importantly, *on a co-moving frame*. Using optimization solvers, we first numerically find a periodic (over a single period) orbit $\boldsymbol{u}(t)$ of the system on a co-moving reference frame. We then cast the linearization along this orbit on a co-moving reference frame as follows:

$$\dot{\boldsymbol{p}} = DF[\boldsymbol{u}, t]\,\boldsymbol{p}. \tag{9}$$

This system of equations for the perturbation along all directions corresponds to a linear system of ODEs with periodic coefficients (through the periodic orbit $\boldsymbol{u}$), where $\boldsymbol{p}(t)$ is the vector determining the direction and size of the perturbation in perturbation space. In practice, since the orbit $\boldsymbol{u}(t)$ can only be found numerically, an explicit form for the above ODE is not readily available. Therefore, we have to recur to numerical integration of the above system of ODEs with the numerically pre-computed orbit $\boldsymbol{u}(t)$. We thus construct numerically the corresponding Jacobian by introducing an initial small perturbation along a chosen dynamical direction and measure the rate of change for all dynamical directions over a period (again, in a co-moving reference frame). Repeating this initial small perturbation along all possible directions allows us to build, column-by-column, the numerical Jacobian. This procedure allows us to numerically compute the eigenvalues for the discrete map induced by perturbations on the dynamics over one period (in the co-moving frame), the so-called Floquet multipliers. We then extract the corresponding stability eigenvalue spectrum by taking the logarithm of these Floquet multipliers. In what follows we use these stability eigenvalues to probe for instabilities. In particular, stability eigenvalues with positive real parts correspond to dynamical instabilities for the co-moving periodic orbits.

C. $\mathcal{K} = 2$ Unbounded Domain Stability

For the unbounded domain case, using the numerical methods explained above, we examine the stability for $\mathcal{K} = 2$ VKVS orbits on n unit cells. Figure 15 depicts the stability spectra as the number of periodic cells n is increased. Interestingly, the most unstable mode is already

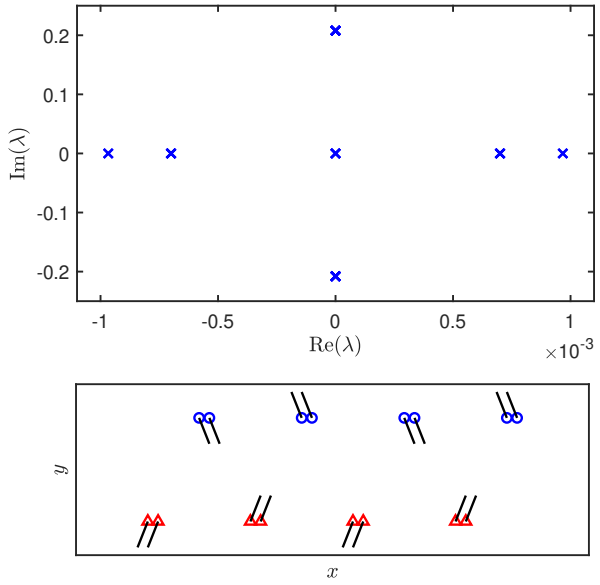

FIG. 16: Example of the eigenvalue spectra (top) and the most dominant eigenvector (bottom, on a visually scaled vortex street) for the case where $a = 20$, $b = 20$, and $d = 0.1$. We note the characteristic Hamiltonian distribution of the eigenvalues, as well as the sawtooth (zig-zag) mode instability being seen in the most unstable mode (which correspond to a repeated pair of real eigenvalues $\lambda = \pm 0.00097$).

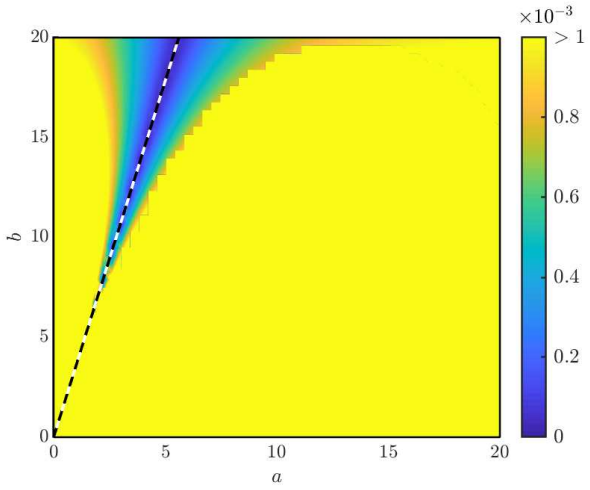

FIG. 17: (Color online) Stability diagram for a $\mathcal{K} = 2$ vortex street in the unbounded domain (no channel walls present) using 2 unit cells and $\Delta\theta = \pi/2$. Depicted is the largest real eigenvalue across a and b with $d = 0.1$. We note a stability region about the VK ratio (see dashed line). The stability diagram corresponding to $d = 1$ is depicted in the bottom panel of Fig. 18.

picked up for $n = 2$. In fact, our numerics show a notable convergence of the maximum real part of the eigenvalue with a relative variation below 10^{-10} (i.e., at the level of the precision for our numerical eigenvalue computations) across all the values of n shown in the figure. This strongly suggests that the most unstable mode is safely picked when using $n = 2$ unit cells. Therefore, from now on, we restrict our analysis to the $n = 2$ cell case as we are focusing on the actual stabilization of these configurations. Examining the eigenvectors corresponding to the most unstable eigenvalues for a wide variety of a and b values, we see that the most unstable mode corresponds to a "sawtooth" mode, where alternating like-signed pairs are both moved in opposite directions (see Fig. 16). This result is tantamount to the instabilities observed in the $\mathcal{K} = 1$ VKVS case where the most unstable mode corresponds to a zig-zag, or pairing, instability mode [3, 19]. Note that in order to capture this most unstable mode with our periodic cell methodology one requires a minimum of two unit cells. This, in turn, explains the strong convergence of the maximum real part of the stability spectrum when using two or more unit cells.

We now consider the two unit cells case ($n = 2$) to compute the stability diagram for VKVSs consisting of $\mathcal{K}$-gon vortex clusters. In particular, as shown in Fig. 17, we find that the $\mathcal{K} = 2$ unbounded street case for $\Delta\theta = \pi/2$ strongly correlates with the stability diagram of the $\mathcal{K} = 1$ street. More important to the stability is varying b, which decreases the largest real eigenvalue component. We explain the dominance of b by noting that an increase in b will correspond to an increase in distance between both positive and negative pairs, while increasing a will increase the distance between opposite-sign pairs but have no effect on the distance between like-signed. Quantitatively speaking, for any given vortex pair, the nearest opposite-signed pair is $\sqrt{4a^2 + b^2}$ away, while the nearest like-signed is $2b$ away. Therefore, as b is increased, the effect of vortex pairs on each other will converge to zero, lowering the magnitude of the effect of any perturbation. Clearly, the $\mathcal{K} = 2$ case retains, to some degree, the behavior of the $\mathcal{K} = 1$ phenomenology. For instance, stability is minimized along the VK ratio. Thus, as intuitively expected, when the vortices are positioned such that the vortex pairs do not noticeably interfere with the orbits of the other vortex pairs (i.e., d being relatively small when compared to a and b, or more precisely to $\sqrt{4a^2 + b^2}$ and $2b$; see above), the street will have an overall behavior resembling the $\mathcal{K} = 1$ case.

In Fig. 18 we contrast the stability diagram for $\Delta\theta = 0$ and $\Delta\theta = \pi/2$ for $d = 1$. Notably, we find that the system has enhanced stability for smaller a and b values along the VK ratio when $\Delta\theta = \pi/2$ than when all pairs are initially given the same rotational angle ($\Delta\theta = 0$). The improvement in stability for $\Delta\theta = \pi/2$ can be explained by noting that the interaction between individual vortices in separate pairs can be minimized by effectively positioning the vortex pairs out-of-phase (i.e., $\Delta\theta = \pi/2$).

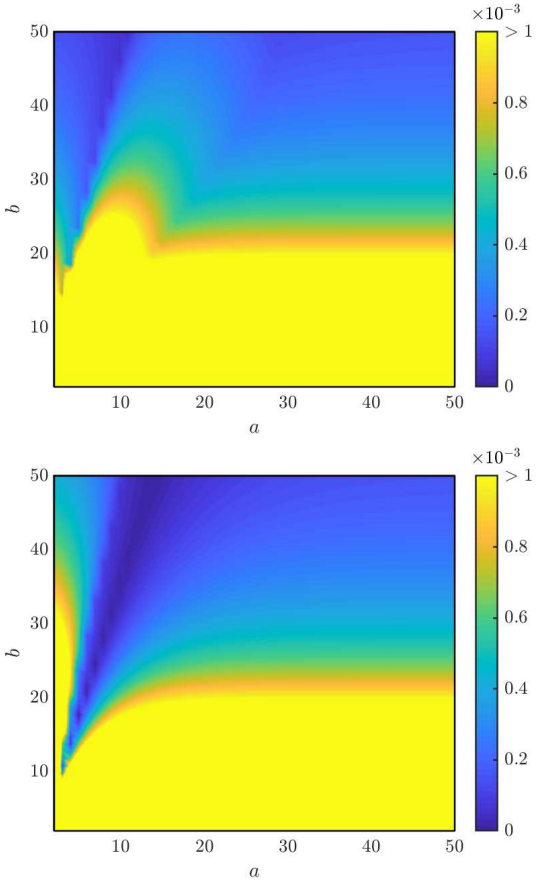

FIG. 18: (Color online) Stability diagram for a $\mathcal{K} = 2$ vortex street in the unbounded domain as in Fig. 17 but for $d = 1$ and $\Delta\theta = 0$ (top) and $\Delta\theta = \pi/2$ (bottom).

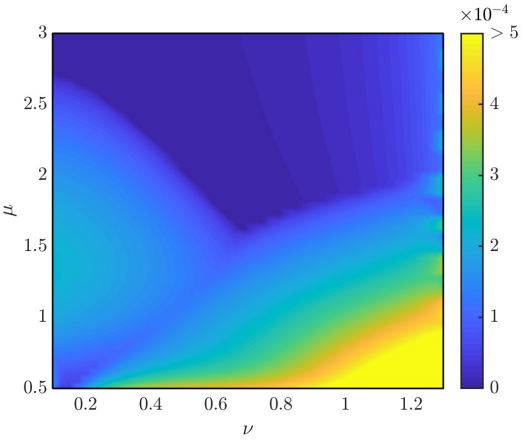

FIG. 19: (Color online) Stability diagram for a $\mathcal{K} = 2$ vortex street in a channel for $d = 0.1$, $c = 100$, and $\Delta\theta = \pi/2$.

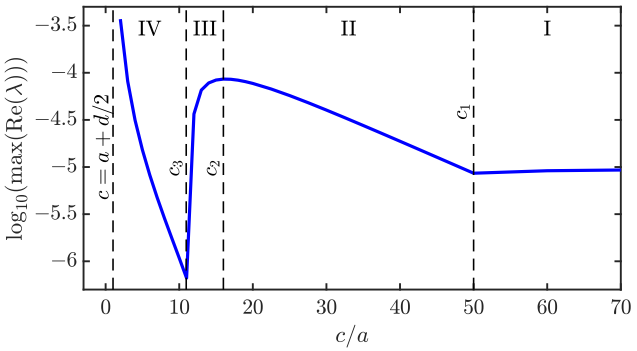

FIG. 20: Effect of varying (half) the channel width c on the stability of a $\mathcal{K} = 2$ vortex street with $a = 10$, $b = 100$, $d = 0.1$, and $\Delta\theta = \pi/2$. Depicted is the largest real part of the eigenvalue spectrum as a function of c normalized by a. The case $c = a + d/2$ (see leftmost dashed vertical line) corresponds to a channel that is perfectly tight on the vortex street. See text for explanation on the four different regions.

D. $\mathcal{K} = 2$ Periodic Channel Stability

We now extend the stability analysis to the channel case. We depict in Fig. 19 the stability diagram for a $\mathcal{K} = 2$ VKVS with $d = 0.1$, $c = 100$, and $\Delta\theta = \pi/2$. We see that, for this relatively small d value, the stability diagram imitates that of the $\mathcal{K} = 1$ channel case. Namely, for low μ and ν parameter values we see a similar stability behavior as in the unbounded domain case: reduced instability along the VK ratio and the instability decreasing as b (μ) increases. For high ν, the channel wall effects override the vortex pair interactions and the $\mathcal{K} = 2$ case is unstable, seen as a sharp increase in the greatest real eigenvalue. Beyond the previous two cases, where the scaled parameters are high enough that the effect of the channel is large, the behavior of the system resembles that of the $\mathcal{K} = 1$ in the channel. On the other hand, we note that the impact of varying d is to destabilize the system for d large relative to the parameter spacing; while the stability region can still be recreated, it requires larger b values for each pair to be considered as a single vortex with respect to the other pairs (see bottom panel of Fig. 18 corresponding to $d = 1$ while Fig. 19 corresponds to $d = 0.1$).

On the other hand, varying the channel width and keeping the $\mathcal{K} = 2$ VKVS parameters constant (a, b, and d), will elucidate the overall stabilization effects due to the presence of the channel. Figure 20 depicts the largest real part of the eigenvalue spectrum as a function of (half) of the channel width c (normalized by a). As the figure shows, there is a complex dependence of the stability on the channel width. Namely, one can discern four qualitatively different regions that can be explained as follows. (I) For large c ($c > c_1$) the effects of the channel are negligible and the $\mathcal{K} = 2$ pair behaves like a single vortex of charge 2Γ. In this case one recovers the stability of the $\mathcal{K} = 1$ VKVS. (II) For intermediately large c ($c_2 < c < c_1$) the channel starts having a noticeable effect on the $\mathcal{K} = 2$ pair despite this being a destabilizing effect. In this c-range, the instability grows by about one order of magnitude. (III) For intermediately moderate c values ($c_3 < c < c_2$) the channel provides a *stabilizing*

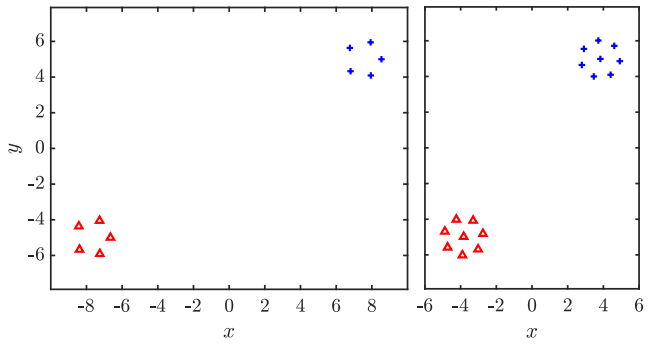

FIG. 21: Examples of larger coherent vortex clusters for $\mathcal{K} = 5$ (left) and $\mathcal{K} = 7{+}1$ (right) obtained through our numerical fixed point routines. In the $\mathcal{K} = 7{+}1$ case, the natural instability of a vortex octagon is counteracted by placing the eighth vortex at the center.

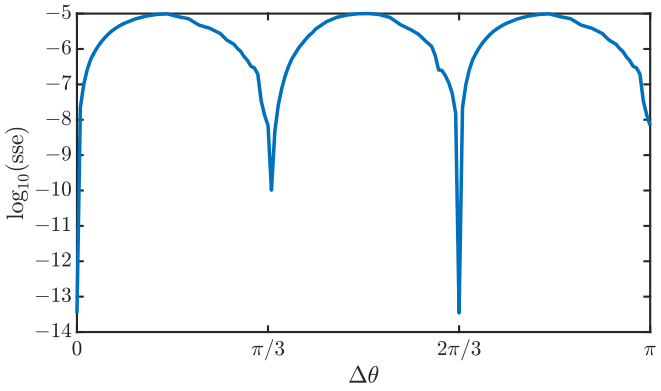

FIG. 22: Same as in Fig. 14 but for the $\mathcal{K} = 3$ case (i.e., equilateral triangle vortex clusters). We observe convergence of the $\mathcal{K} = 3$ VKVS when the relative angle between the equilateral triangles is a multiple of $\pi/3$.

effect of the $\mathcal{K} = 2$ VKVS. This stabilizing effect reduces the instability by two orders of magnitude. (IV) Finally, for small c values ($c < c_3$) the channel starts to interfere with the $\mathcal{K} = 2$ pair and completely destabilizes the VKVS solution. This region ceases to exist when c approaches a (or more precisely $a + d/2$) where the pair "hits" the channel walls. The complex, non-monotonic, dependence of the stability on the channel width suggest that each type of instability (i.e., each unstable eigenvector) is affected in a different manner as the channel is tightened.

To summarize, the $\mathcal{K} = 2$ VKVS is shown to be most stable for values that correspond to the VK ratio in an unbounded domain. The addition of the channel provides enhanced stability for carefully chosen channel widths ($c_3 < c < c_2$) but otherwise might be detrimental towards stabilization. Despite the fact that small instabilities are always present in the $\mathcal{K} = 2$ case, as these instabilities are weak (of the order of 10^{-6}) in some regions, direct numerical integrations for long times suggest that these $\mathcal{K} = 2$ VKVS configurations may be long-lived for physically realistic time scales.

E. $\mathcal{K} > 2$ Cases

Employing point-vortex models to represent more complex VKVS states may be further extended to cover cases with greater numbers of vortices. We note that for an isolated $\mathcal{K}$-gon of point vortices, cases where $\mathcal{K} > 7$ are always unstable [22, 26–28]. Therefore, to construct long-lived VKVS configurations with vortex clusters consisting of regular $\mathcal{K}$-gons, one must choose $\mathcal{K} \leq 7$. Beyond seven vortices, larger constructs can be created and form periodic orbits, but it requires more complicated geometries. These geometries include the so-called $N + 1$ vortex configurations consisting of a regular polygon of N vortices with an extra single-charged vortex at the center [31] or even semi-concentric polygonal rings of vortices [32, 33]. For instance, Fig. 21 depicts VKVS configurations with higher $\mathcal{K}$ values obtained through our numerical fixed point iteration routines. Specifically, the figure shows a $\mathcal{K} = 5$ VKVS (left) with a regular pentagonal vortex clusters and a $\mathcal{K} = 7{+}1$ VKVS consisting of a regular septagon with an extra (single) vortex at is center.

Similarly, we find that for higher values of $\mathcal{K}$, the streets exist most clearly when $\Delta\theta = n\pi/\mathcal{K}$ (see for instance the convergence results for the $\mathcal{K} = 3$ case in Fig. 22). The result is that the system tends towards two broad states, given that the states are identical across even and odd values of n which correspond, respectively, to in-phase and out-of-phase $\mathcal{K}$-gons between the positively and negatively charged clusters. Given the results from the $\mathcal{K} = 2$ case, we predict that the configuration corresponding to $\Delta\theta = \pi/\mathcal{K}$ will be stable for relatively low values of a and b, and thus will be more readily observable.

VII. DISCUSSION AND CONCLUSIONS

In this work we extend the results on the standard von-Kármán (VK) vortex street (VKVS) with and without a confining channel by implementing a reduced point-vortex ODE model that dynamically generates a vortex street. This model is tantamount as how these vortex streets are created in nature at the wake of an impurity moving through a fluid. These dynamically generated wakes inherit their stability from the fully formed, infinite VKVS. For instance, we are able to generate stable wakes around the so-called VK ratio between horizontal and vertical spacings between vortices. In case of instability, the tail-end of the VKVS breaks into a disordered (chaotic) collection of vortices.

We also generalize the concept of a VKVS by replacing each vortex by a small cluster of $\mathcal{K}$ co-rotating vortices. In its simpler form, these clusters correspond to a regular $\mathcal{K}$-gon. We study the existence and stability of the

$\mathcal{K} = 2$ VKVS case comprised of co-rotating vortex pairs. We find that the $\mathcal{K} = 2$ VKVS inherits the stability properties of its $\mathcal{K} = 1$ counterpart when the diameter of each pair is relatively small compared to the distance between pairs. In particular, we find that $\mathcal{K} = 2$ VKVSs are stable for relatively large values of the horizontal separation (compared to the channel width) and along the VK ratio. This stability is progressively lost as the diameter of the vortex pair increases. We also note that the $\mathcal{K} = 2$ (or in general for any $\mathcal{K}$) VKVS has, in addition to the size of the $\mathcal{K}$-cluster, an extra shape parameter as oppositely charged clusters may be placed at an angle $\Delta\theta$ with respect to each other. Our results suggest that the case of $\Delta\theta = \pi/2$ has enhanced stability when compared to the $\Delta\theta = 0$ case. This is explained by the fact that in the $\Delta\theta = \pi/2$ case, the vortices across clusters are kept further away during evolution (i.e., weaker interactions) than when $\Delta\theta = 0$.

On the other hand, our results reveal, for certain shape parameter combinations, a complex dependence of the stability of the $\mathcal{K} = 2$ VKVS on the channel width. In particular we have shown cases where the stability is described by four different regions as follows: for large channel width the $\mathcal{K} = 2$ VKVS mirrors the stability of the $\mathcal{K} = 1$ VKVS; for intermediately large channel width the channel has a destabilizing effect; for intermediately moderate channel widths there exist small intervals where the channel *enhances* stability; and finally, as the channel becomes too tight to the VKVS, large instabilities ensue as the vortices get too close to the channel walls. This complex dependence is attributed to the different unstable eigenmodes being affected differently by the presence of the channel.

Also, our analysis suggests that the appearance of the $\mathcal{K} = 2$ VKVS instead of the $\mathcal{K} = 1$ VKVS in Bose-Einstein condensates is not due to a combination of instability of the $\mathcal{K} = 1$ with stability (or weaker instability) of the $\mathcal{K} = 2$ VKVS. In fact, our results suggest that a $\mathcal{K} = 2$ VKVS will always be more unstable than its $\mathcal{K} = 1$ counterpart. However, our study does not reveal why indeed $\mathcal{K} = 2$ are prevalent in Bose-Einstein condensates. We postulate that, in this case, the generation of the $\mathcal{K} = 2$ VKVS, instead of the $\mathcal{K} = 1$, is due to the way the vortices are generated around the impurity. For instance, it is possible that a symmetry breaking mechanism could be responsible for the early generation of a single vortex close to the impurity. Close proximity to the impurity will induce the vortex to quickly migrate along the periphery of the impurity (due to the effects of its mirror image) and pair up with another vortex on the other side of the impurity thus creating the $\mathcal{K} = 2$ pair. This pertinent speculation deserves further consideration.

We point to the possibility of creating VKVSs comprised of larger clusters of vortices. These clusters, if stable on their own right (i.e., when isolated), might replace each vortex in the $\mathcal{K} = 1$ VKVS to create a VK vortex-cluster street. Our preliminary analysis suggests that VKVSs comprised of $\mathcal{K}$-gons only exist when positively and negatively charged $\mathcal{K}$-gons are in-phase ($\Delta\theta = 0$) or out-of-phase ($\Delta\theta = \pi/\mathcal{K}$). It would be relevant to study in more detail the stability properties of VKVSs comprised of $\mathcal{K}$-gons (or other stable tight clusters like the concentric-type polygons cataloged in Refs. [32, 33]) with larger values of $\mathcal{K}$. In the same vein, even at the level of existence, it would be interesting to study VKVSs comprised of positively-charged clusters that are different than the negatively-charged ones. For instance, it is interesting to ask whether the total charge of each of these clusters should be same in order to support a steady state. Work in these directions is under way and will be reported in a future publication.

Finally, it is worth mentioning that a helical vortex [34] has a transverse cut that is precisely a VKVS. Therefore, one could consider VKVSs as the low-dimensional (2D) cousin of 3D helical vortices and thus their properties could be related. For instance, a prevalent destabilization mode observed in helical vortices correspond to the sawtooth (zig-zag) mode [35] that is precisely one of the most unstable modes identified in our work. Furthermore, $\mathcal{K} > 1$ streets also have their higher-dimensional equivalent in the form of interlaced helical vortices [36]. The intriguing connection between VKVSs and helical vortices could be exploited to elucidate some configurational and dynamical properties (i.e., stability) for the latter.

Acknowledgments

R.C.G. gratefully acknowledges support from the US National Science Foundation under grant PHY-1603058.

[1] H. Lamb, in *Hydrodynamics* (Dover, New York, 1945).
[2] T. von Kármán, Prog. Aerosp. Sci. **59**, 13 (2013).
[3] T. von Kármán, Prog. Aerosp. Sci. **59**, 16 (2013).
[4] L. Rosenhead, Proc. Royal Soc. Lond. **228**, 275 (1929).
[5] K. Sasaki, N. Suzuki, and H. Saito, Phys. Rev. Lett. **104**, 150404 (2010).
[6] G.W. Stagg, N.G. Parker, and C.F. Barenghi, J. Phys. B: At. Mol. Opt. Phys. **47**, 095304 (2014).
[7] C. Huepe and M.-E. Brachet, Physica D **140**, 126–140 (2000).
[8] F. Lin and J. Wei, Disc. Cont. Dyn. Syst. A **39**, 6801–6824 (2019).
[9] T. Schnipper, A. Andersen, and T. Bohr, J. Fluid Mech. 633, 411–423 (2009).
[10] M.A. Stremler and M. Brøns, Proc. Appl. Math. Mech. **7**, 1101305 (2007).

[11] M.A. Stremler, A. Salmanzadeh, S. Basu, and C.H.K. Williamson, J. Fluids Struct. **27**, 774–783 (2011).
[12] M.A. Stremler and S. Basu, Fluid Dyn. Res. **46**, 061410 (2014).
[13] S. Basu and M.A. Stremler, Phys. Fluids **27**, 103603 (2015).
[14] M.A. Stremler and S. Basu, J. Fluid Mech. **831**, 72 (2017).
[15] W.J. Kwon, J.H. Kim, S.W. Seo, and Y. Shin, Phys. Rev. Lett. **117**, 245301 (2016).
[16] P. Boniface, L. Lebon, L. Limat, and M. Receveur, Europhys. Lett. **117**, 34001 (2017).
[17] J. Jiménez, J. Fluid Mech. **178**, 177–194 (1987).
[18] P. G. Saffman and J. C. Schatzman, J. Fluid Mech. **117**, 171–185 (1982).
[19] S. Kida, J. Fluid Mech. **122**, 487–504 (1982).
[20] D. I. Meiron, P. G. Saffman, and J. C. Schatzman, J. Fluid Mech. **147**, 187–212 (1984).
[21] S. Mowlavi, C. Arratia, and F. Gallaire, J. Fluid Mech. **795**, 187-209 (2016).
[22] P. Newton, *The N-vortex problem: analytical techniques*, Springer-Verlag, New York, 2001.
[23] See, e.g., P.K. Kundu, I.M. Cohen, and D.R. Dowling, *Fluid Mechanics* (Elsevier, Waltham, 2012).
[24] L. Greengard, SIAM J. Sci. Comput. **11**, 603 (1990).
[25] H. Rubach and T. von-Kármán, NASA. Ames Res. Center Classical Aerodyn. Theory, 57 (1979).
[26] T. Havelock, Philos. Mag. **11**, 617 (1931).
[27] L.G. Kurakin and V.I. Yudovich, Dokl. Phys. **47**, 465–470 (2002).
[28] L.G. Kurakin and V.I. Yudovich, Chaos **47**, 465 (2002).
[29] M.A. Stremler, Theor. Comp. Fluid Dyn. **24**, 25–37 (2010).
[30] R. Castelli and J.-P. Lessard SIAM J. Appl. Dyn. Syst. **121**, 204–245 (2013).
[31] H. Cabral and D. Schmidt, SIAM J. Math. Anal. **31**, 231 (2000).
[32] L.J. Campbell and R.M. Ziff, Los Alamos Scientific Laboratory Report No. LA-7384-MS (1978);
[33] L.J. Campbell and R.M. Ziff, Phys. Rev. B **20**, 1886 (1979).
[34] O. Velasco Fuentes J. Fluid Mech. **836**, R1 (2017).
[35] O. Velasco Fuentes, private communication.
[36] O. Velasco Fuentes J. Fluid Mech. **842**, R2 (2018).